Engineering Out Motion: Introduction of a de Novo Disulfide Bond and a Salt Bridge Designed To Close a Dynamic Cleft on the Surface of Cytochrome b_5[†]

Elizabeth M. Storch, Valerie Daggett,* and William M. Atkins*

Department of Medicinal Chemistry, University of Washington, Seattle, Washington 98195-7610

Received September 8, 1998; Revised Manuscript Received February 2, 1999

ABSTRACT: A previous molecular dynamics (MD) simulation of cytochrome b_5 (cyt b_5) at 25 °C displayed localized dynamics on the surface of the protein giving rise to the periodic formation of a cleft that provides access to the heme through a protected hydrophobic channel [Storch and Daggett (1995) *Biochemistry 34,* 9682]. Here we describe the production and testing of mutants designed to prevent the cleft from opening using a combination of experimental and theoretical techniques. Two mutants have been designed to close the surface cleft: S18D to introduce a salt bridge and S18C:R47C to incorporate a disulfide bond. The putative cleft forms between two separate cores of the protein: one is structural in nature and can be monitored through the fluorescence of Trp 22, and the other binds the heme prosthetic group and can be tracked via heme absorbance. An increase in motion localized to the cleft region was observed for each protein, except for the disulfide-containing variant, in MD simulations at 50 °C compared to simulations at 25 °C. For the disulfide-containing variant, the cleft remained closed. Both urea and temperature denaturation curves were nearly identical for wild-type and mutant proteins when heme absorbance was monitored. In contrast, fluorescence studies revealed oxidized S18C:R47C to be considerably more stable based on the midpoints of the denaturation transitions, T_m and $U_{1/2}$. Moreover, the fluorescence changes for each protein were complete at ∼50 °C and a urea concentration of ∼3.9 M, significantly below the temperature and urea concentration (62 °C, 5 M urea) required to observe heme release. In addition, solvent accessibility based on acrylamide quenching of Trp 22 was lower in the S18C:R47C mutant, particularly at 50 °C, before heme release [presented in the accompanying paper (*58*)]. The results suggest that a constraining disulfide bond can be designed to inhibit dynamic cleft formation on the surface of cyt b_5. Located near the heme, the native dynamics of the cleft may be functionally important for protein−protein recognition and/or complex stabilization.

Cytochrome b_5 (cyt b_5)[1] is a heme-containing protein that participates in electron-transfer reactions with a variety of redox partners (Figure 1). Cyt b_5 occurs naturally in both soluble and membrane-bound forms. The soluble form is found in erythrocytes and reduces hemoglobin (*1, 2*). The membrane-bound form is located in the endoplasmic reticulum (ER) and mitochondria. In the ER, ferric cyt b_5 is reduced by either NADH−cyt b_5 reductase or NADPH−cytochrome P450 reductase. The ferrous form of the protein reduces various fatty acyl coenzyme A desaturases for the biosynthesis of selected lipids and donates an electron to certain cytochrome P450s in their catalytic reaction cycle (*3, 4*). In the mitochondria, cyt b_5 participates in electron transfer from NADH to cytochrome *c* oxidase via cytochrome *c* (*5*). Cyt b_5 has been studied most extensively as a soluble tryptic fragment. This form of the protein retains the heme and transfers electrons, in vitro, with both physiological and nonphysiological redox partners. Because cyt b_5 par-

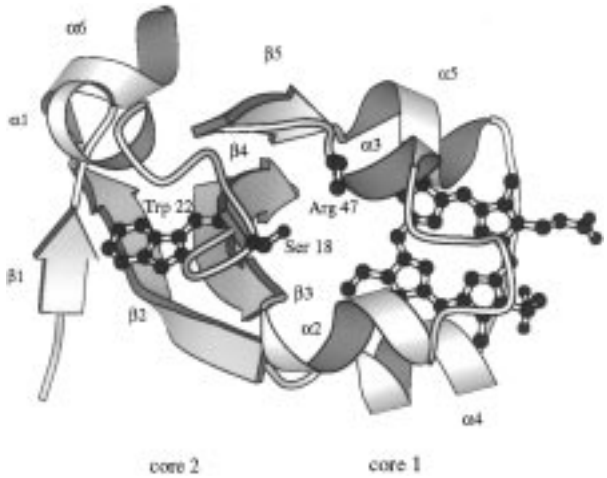

FIGURE 1: Ribbon diagram of the crystal structure of cyt b_5 (*25*). The prosthetic heme group, Ser 18, Trp 22, and Arg 47 positions are shown in stick representation. The proposed cleft region lies between residues 18 and 47. The residues involved in secondary structure are α1 (9−12), α2 (33−38), α3 (44−47), α4 (55−60), α5 (65−71), α6 (81−86), β1 (5−7), β2 (74−80), β3 (27−32), β4 (21−25), and β5 (51−54). The numbering scheme for bovine cyt b_5 is used.

[†] Supported by the National Institutes of Health (GM 50789 to V.D.), the Department of Medicinal Chemistry, and Merck Research Labs (to W.M.A.).

* Address correspondence to either author. FAX: (206) 685-3252. Phone: (206) 543-7025. E-mail: daggett@fitz.mchem.washington.edu. E-mail: winky@u.washington.edu.

[1] Abbreviations: cyt b_5, cytochrome b_5; ER, endoplasmic reticulum; MD, molecular dynamics; S18C:R47C$_{ox}$, oxidized S18C:R47C; S18C:R47C$_{red}$, reduced and acetylated S18C:R47C; DTT, dithiothreitol; β-ME, β-mercaptoethanol; λ_{mass}, spectral center of mass; RMS, root-mean-squared; NOEs, nuclear Overhauser effect cross-peaks; *N*, native state; *N′*, predenatured state; *D*, denatured state.

10.1021/bi982158q CCC: $18.00
Published on Web 04/02/1999

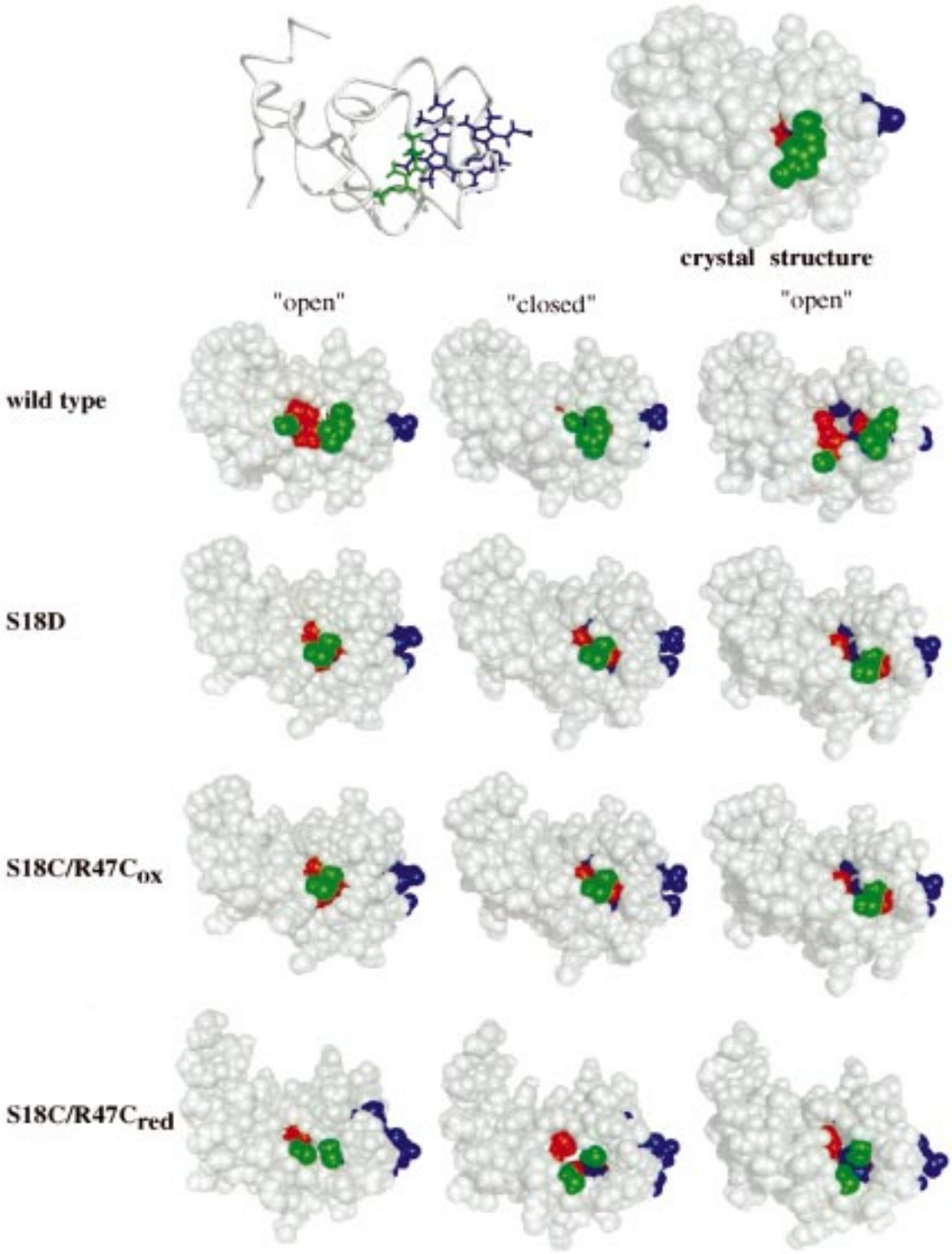

FIGURE 2: Space-filling representations of cyt b_5 depicting control of the 'opened' and 'closed' conformations of the cleft in the wild type (*6*), S18D, S18C:R47C$_{ox}$, and S18C:R47C$_{red}$ MD simulations. The buried hydrophobic residues that intermittently became exposed upon cleft formation are colored red, and include the backbone of Trp 22. The residues in green (Ser 18 and Arg 47) were mutated in our experiments. The prosthetic heme group is colored blue.

ticipates in electron-transfer reactions with a variety of different proteins, it is of interest to determine the molecular basis of the cross-reactivity and recognition events.

Molecular dynamics (MD) simulations suggest that tryptic-solubilized cyt b_5 has persistent areas of localized motion (*6*), resulting in the intermittent formation of a large cleft that exposes portions of the hydrophobic interior and the heme group (Figure 2). Recent ^{1}H NMR studies on rat microsomal cyt b_5 (*7*) provide support for the localized motion observed by MD. The location of the cleft is at the interface of the two cores of cyt b_5 (Figures 1 and 2), and both experimental studies (*8*−*12*) and MD simulations (*13*) of apocyt b_5 suggest that the two cores are structurally independent. Consequently, the observed fluctuations in the cleft region of the holoprotein may be important to stability and possibly function.

Previous experimental results, based on crystallographic models, predict limited solvent accessibility of the heme through one edge of the prosthetic group (*14*). Therefore, most models of protein−protein interactions with redox partners have focused on a single anionic patch surrounding the exposed heme edge on the surface of cyt b_5 (*14*−*19*). The cleft formation predicted by MD provides an additional route of access to the heme group that cannot be predicted a priori from static crystal structures or models of complexes. In addition, the cleft is in close proximity to many of the acidic residues implicated experimentally in protein−protein complex formation (*20*−*24*). Together these results suggest that this region of the protein may be of functional importance in biological redox processes, as well as in maintenance of a stable, native conformation.

Here we have introduced mutations in cyt b_5 in an attempt to alter and thereby test cleft formation. Using computer modeling and mutagenesis, we designed and produced two cyt b_5 mutants aimed to restrict the cleft fluctuations: an S18D mutant (proposed to form a salt bridge with Arg 47) and a disulfide mutant (designed to covalently close the cleft). The disulfide mutant was expected to exhibit different dynamics in the oxidized and reduced states (S18C:R47C$_{ox}$ and S18C:R47C$_{red}$, where ox and red refer to the disulfide oxidation states). MD simulations of the wild-type and mutant proteins were performed at 25 and 50 °C. Simulations under these conditions provide detailed information about the structural and dynamic consequences of the mutations prior to heme loss. The effects of the mutations on equilibrium stability were also investigated experimentally via urea and thermal denaturation. We have employed two spectroscopic probes of structural perturbations that flank the putative cleft region: heme absorbance (which reports on core 1) and fluorescence of Trp 22 (reporting on core 2) (Figure 1).

The mutations had only modest effects on heme binding, as determined by absorbance spectroscopy; however, they had pronounced effects on the steady-state fluorescence of Trp 22 prior to heme release. The two probes indicate that there are conformational changes in the native state (*N*) that occur prior to heme expulsion. These conformational changes appear to be linked to the cleft on the basis of the MD simulations and the lack of such effects when the cleft is closed covalently with a disulfide bond. Taken together, the results presented here demonstrate that the dynamics and conformational behavior of cyt b_5 can be rationally controlled.

MATERIALS AND METHODS

Molecular Dynamics Simulations. The starting conformation for the computer simulations was the tryptic-solubilized bovine ferric cyt b_5 crystal structure obtained from the Brookhaven Protein Data Bank (PDB Accession Number 3b5c). The structure was determined by Mathews and co-workers to 1.5 Å resolution (*25*). The crystal structure contains residues 3−87; residues 1−2 and 88−93 are not visible in the electron density maps and were therefore omitted in the starting structure for the simulations. For the mutant cyt b_5 simulations, modifications were made to the bovine crystal structure coordinates by placing the new side chains in approximately the same orientation as the wild-type residues: S18D, S18C:R47C$_{ox}$, and S18C:R47C$_{red}$.

Energy minimization and the MD simulations were performed using the program ENCAD (*26*). The potential energy function (*27, 28*) and associated protocols (*29*) are described in detail elsewhere. The heme parameters of Henry and co-workers were used (*30*). The system consisted of the protein in a rectangular box of water molecules with walls at least 8 Å from any protein atom (∼3000 water molecules per simulation). The water density was set to the experimental value of 0.997 g/mL at 298 K or 0.988 g/mL at 323 K by adjusting the volume of the box (*31*). The systems were subjected to a variety of preparatory steps as described elsewhere (*6*). Each simulation was carried out for 2 ns, except the wild-type simulation at 298 K which was performed for 2.5 ns. An 8 Å nonbonded cutoff was used, and the nonbonded list was updated every five steps. Structures were saved every 0.2 ps, and the last nanosecond of each simulation was considered for analysis.

Materials. Enzymes used in the mutagenesis protocols were purchased from New England Biolabs (Beverly, MA). Custom oligonucleotides were purchased nonphosphorylated from National Biosciences, Inc. (NBI, Plymouth, MN), or Life Technologies, Inc. (Gibco BRL, Rockville, MD). P-30 gel filtration resins were obtained from Biorad (Hercules, CA). DEAE Sepharose anionic exchange resins were obtained from Pharmacia Biotech (Piscataway, NJ). All other chemicals were reagent grade.

Site-Directed Mutagenesis. A synthetic rat cyt b_5 gene (99 residues, corresponding to the tryptic-solubilized form) harbored in a pUC13 plasmid was kindly provided by Dr. S. Sligar and is described elsewhere (*32*). Cassette mutagenesis was used to construct the S18D mutant, utilizing the *Pst*I and *Sal*I restriction sites in the synthetic gene. Because of the large distance between these sites, a cassette made of five individual oligonucleotides was used: three wild-type and two mutant complementary oligonucleotides containing the GAC codon (Ser → Asp) and a silent mutation encoding a *Sty*I restriction site to facilitate mutant identification. The oligonucleotides were annealed and ligated into the double-digested plasmid following the protocol described previously (*33*). The S18C:R47C mutant was constructed using the commercially available ClonTech kit (Palo Alto, CA). Two oligonucleotide primers were used: one contained a TGT codon (Ser → Cys) and a silent mutation deleting a native *Sal*I restriction site, and the second primer contained a TGC codon and a silent mutation deleting the native *Nae*I restriction site. The protocols for standard mutagenesis procedures, such as plasmid isolations and transformations, and SDS−PAGE analyses of proteins are published elsewhere (*34*). Dideoxy sequencing was used to confirm successful mutations.

Protein Expression, Purification, and Characterization. E. coli DH5α cells containing pUC13 plasmids harboring the wild-type or mutant cyt b_5 genes were expressed and purified following the method of Stayton and co-workers (*33*). A buffer system of 50 mM K_2HPO_4, 1 mM EDTA, and 0.1 mM dithiothreitol (DTT) (omitted for S18C:R47C) at pH 7 was used. When DTT was included in the S18C:R47C purification, significant heme loss occurred due to decreased stability of heme ligation in the reduced di-cysteine protein (data not shown). Fractions from each chromatographic step with absorbance ratios of 280/412 nm of ≤0.18 were pooled and concentrated. Protein purity was determined by SDS−

PAGE analysis and mass spectrometry. Mass spectrometry experiments were performed on a Perceptive Systems Voyager Elite MALDI-TOF instrument. The mass range scanned was *m*/*z* 1000−45 000 at 337 nm. The matrix consisted of a 50% acetonitrile solution saturated with 95% dihydroxybenzoic acid/5% methoxysalicylic acid. Approximately 5 pmol of protein per sample was analyzed in triplicate. Internal standards were ubiquitin and myoglobin (8565.81 and 16 952.5 Da, respectively). MALDI-TOF indicated that the averaged molecular masses of the proteins were 11 212.4 Da (wild type), 11 240.3 Da (S18D), and 11 173.8 Da (S18C:R47C). These masses are in excellent agreement with values calculated from the amino acid composition of apocyt b_5 minus the N-terminal methionine residue: 11 210.3 Da (wild type), 11 238.3 Da (S18D), and 11 173.3 Da (S18C:R47C). Protein concentrations were determined from the absorbance at 412 nm using an extinction coefficient of 117 mM^{-1} cm^{-1} (*35*).

S18C:R47C Oxidized and Reduced Disulfide Determination. The S18C:R47C protein was subjected to iodoacetic acid modification in the presence or absence of DTT (*36*) to yield oxidized (S18C:R47C_{ox}) and reduced−carboxymethylated (S18C:R47C_{red}) proteins. All reactions contained 0.1 M Tris at pH 8.6 purged with argon. Typically 200 μM protein in 500 μL total volume was used. DTT was added in 10-fold molar excess over protein thiol concentration, while the control contained no DTT, and incubated for 3 h at 37 °C. Iodoacetic acid was added in a 5-fold excess over total thiol concentration, and the mixture was incubated in the dark for 1 h at 37 °C. To this reaction was added β-mercaptoethanol (β-ME) in 10-fold excess over iodoacetic acid concentration, and the mixture was immediately desalted on a P-30 gel filtration column. Modification was determined by MALDI-TOF (as previously described) and nonreducing SDS−PAGE analysis. The reduced and acetylated S18C:R47C was used in the experiments, while the free sulfhydryl form of the protein was used in the MD simulations.

Urea Denaturation. All stock solutions for denaturation studies were prepared in 5 mM K_2HPO_4 at pH 7 and filtered. A final protein concentration of 10 μM was used in all denaturation experiments. Known amounts of 10 M stock urea solution, buffer, and stock protein solution were added to a cuvette and incubated for 15 min for each desired urea concentration. The absorption spectra were measured on a Varian Cary 3E UV−Vis spectrophotometer using matched 1 cm quartz cuvettes at a temperature of 25 °C. Absorption denaturation curves were constructed by plotting the absorption at 412 nm versus the molar concentration of urea. The fluorescence spectra were measured on an SLM-8100 fluorometer using 1 cm quartz cuvettes at a temperature of 25 °C. The excitation wavelength was 295 nm using a detection cutoff filter of 305 nm. The slit widths were 4−8 nm. Fluorescence denaturation curves were constructed by plotting the spectral center of mass in nanometers ($\lambda_{mass} = 1/\sum \nu_i F_i / \sum F_i$, where F_i is the fluorescence intensity at wavenumber ν_i) or the intensity of the intrinsic fluorescence of proteins versus the molar concentration of urea. The data were analyzed as described by Pace (*37*), and curves were fit to the following equations taking sloping base lines into account. Assuming a two-state denaturation mechanism, the equilibrium constant, K_{eq}, was estimated by the equation: $K_{eq} = [A_n(U) - A(U)]/[A(U) - A_d(U)]$. Values $A_n(U)$ and $A_d(U)$ were absorbance or fluorescence values of the native and denatured proteins, respectively, at urea concentration U, and $A(U)$ is the measured absorbance or fluorescence at a specific urea concentration. The standard free energy difference between the native and denatured conformations was calculated by: $\Delta G_{app} = -RT \ln (K_{eq})$. A linear dependence of ΔG_{app} on denaturant concentration was assumed: $\Delta G_{app} = \Delta G_{app}(H_2O) - m[U]$, where $\Delta G_{app}(H_2O)$ is the standard free energy difference between native and denatured forms of cyt b_5 in the absence of urea and m reflects the sensitivity of the transition region to denaturant concentration.

Temperature Denaturation. The buffer conditions, instrumentation, and setup were the same as described for the urea denaturation experiments. High-temperature 1 cm quartz cuvettes with Teflon stoppers and stir bars were used to prevent evaporation. Samples were heated in increments of 2.5 °C from approximately 20 to 95 °C and equilibrated for 10 min at each temperature before collecting spectral data. Thermal denaturation curves were fit to an equation that accounts for base lines with nonzero slopes (*38*).

RESULTS

Molecular Dynamics Characterization of Wild-Type and Mutant Proteins. MD simulations were performed in order to design mutants in which the state of the putative cleft could be controlled and provide a structural basis for the experimental denaturation studies (Figure 2). In Figure 2, the dynamics of the cleft region are compared for wild type, S18D, S18C:R47C_{ox}, and S18C:R47C_{red} proteins. Residues in the hydrophobic cleft (red) that are transiently exposed in the wild-type remain unexposed in the S18D and S18C:R47C_{ox} proteins. Reduction of the disulfide, in S18C:R47Cred, leads to a persistent, partially opened, cleft. Each simulation was performed for 2 ns in water and yielded similar overall C_α root-mean-squared (RMS) deviations from the crystal structure at 25 °C of ∼2.4 Å, with the exception of S18D which was ∼3 Å. The motion, however, was distributed differently along the backbone in each of the proteins. At 50 °C, the wild-type protein yielded the largest C_α RMS deviation (∼3.8 Å) from the crystal structure, while the deviations for the mutants were ∼3 Å.

While deviations from the crystal structure may be useful for assessing simulations, it is possible to obtain high RMS deviations and quantitatively reproduce NMR data of solution structures. This is the case for wild-type cyt b_5 (*6*). Therefore, tertiary contacts were monitored throughout the simulation and compared to experimental NMR data. Potential nuclear Overhauser effect cross-peaks (NOEs) were evaluated by calculating an average-weighted distance ($<r^{-6}>^{-1/6}$) between interacting hydrogens during the simulation. The validity of the simulations was determined by how well the experimentally determined NOEs were retained (*8, 11*). All of the hydrogen−hydrogen distances corresponding to the core 2 NOEs [see Figure 4 of Moore and Lecomte, (*8*)] remained below 5 Å, which is considered a reasonable cutoff for an NOE (*39*). Most of these NOEs are present even in the more structurally dynamic apoprotein (*8, 13*), and they were, therefore, expected to be present in mutant forms of the holoprotein. At 25 °C, NOEs between β-strands 4 and 5 ($d_{\alpha N}$ connectivities between residues 23 and 51 and 23 and

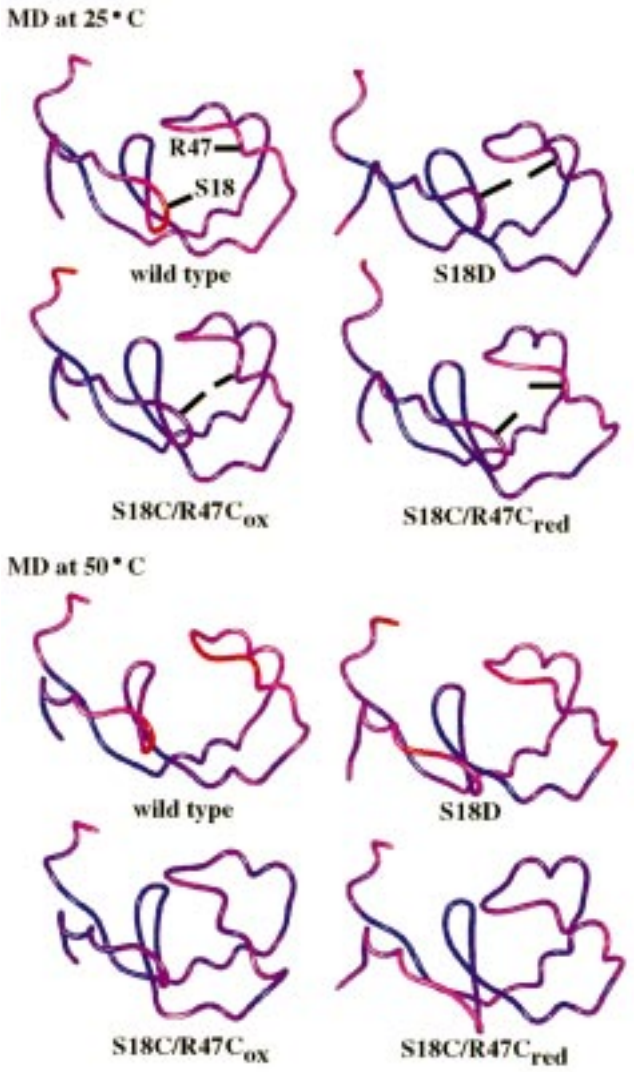

FIGURE 3: Main-chain C_α traces of cyt b_5 depicting relative mobility as determined from the C_α RMS fluctuation from the last 1 ns of the simulations. Orientation is the same as in Figure 1, but the heme is not displayed. Structures are colored according to relative motion from blue (low mobility) to red (high mobility). (A, top) Mean structures from MD simulations at 25 °C. (B, bottom) Mean structures from MD simulations at 50 °C.

52) were intermittently lost in the mutant protein simulations. This separation of the strands was most likely due to strain introduced by the nearby mutations. These contacts are labile in the apoprotein simulations and in some of the recent ^{1}H NMR studies on microsomal cyt b_5 (*7*). At 50 °C, the $\beta4/\beta5$ NOEs were lost in the wild-type and S18D simulations. Among other structural changes, loss of these contacts allowed initial separation and independence of the cores, particularly in the wild-type protein.

As a measure of internal motion, the C_α RMS fluctuations describing the motion about the mean structure were used to determine the distribution of mobility along the sequence. The average fluctuations for the last 1 ns of each simulation were calculated and are shown mapped onto the calculated mean structures in Figure 3. At 25 °C, the wild-type simulation had the highest mobility in the putative cleft region. Fluctuations were highest in an external loop (residues 14−18), α-helices 2 and 3 (residues 35−49), and the C-terminus (residues 83−85) (*6*). The mutant simulations, however, displayed much lower fluctuations in this area. The S18D simulation showed much less backbone mobility, where the highest fluctuations were in the termini and $\beta5$ (residues 51−52). In the S18C:R47C$_{ox}$ simulation, mobility was restricted to $\beta5$ (residues 51−52) and the C-terminus (residues 85−87). Surprisingly, the S18C:R47C$_{red}$ simulation also showed decreased mobility in α3 (residues 42−52) and the C-terminus (residues 85−87) relative to the wild-type protein. For comparison, the mean structures of the mutants have RMS deviations of 1.9 Å (S18D), 1.4 Å (S18C:R47C$_{ox}$), and 1.4 Å (S18C:R47C$_{red}$) from the mean wild-type structure, where much of this difference was caused by fluctuations in the cleft area.

The C_α RMS fluctuations at 50 °C are shown in Figure 3. The wild-type simulation displayed increases in mobility in the same areas as at 25 °C but extending further along the backbone. Fluctuations in S18D paralleled wild type with additional mobility in α5. The fluctuations in the S18C:R47C$_{red}$ protein also increased with temperature, but to a much lesser degree: increased fluctuations were seen only in α1 and the adjacent loop (residues 9−21) and in $\beta2$ (residues 72−75). In comparison, S18C:R47C$_{ox}$ still showed lower mobility, even at this higher temperature. Both the oxidized and reduced disulfide proteins were ∼2.6 Å from the mean wild-type structure at 50 °C, while the value for S18D was only 1.9 Å. This apparent decrease in fluctuation at 50 °C for S18D compared to wild type is intriguing, but it was not observed by the experimental probes discussed here or in the accompanying paper (*58*). Still, the MD simulations showed decreased mobility in the cleft region upon mutation and suggest that these mutants would be good candidates to test our hypothesis experimentally.

Experimental Characterization of Oxidized and Reduced Forms of the Disulfide Mutant. To confirm the oxidation state of the S18C:R47C mutant, the protein was subjected to thiol alkylation with iodoacetic acid in the presence or absence of DTT, and major protein products were detected by MALDI-TOF. The spectrum of S18C:R47C exposed to iodoacetic acid in the presence of DTT (S18C:R47C$_{red}$) is shown in Figure 4A. The major product at 11 232.9 Da was determined to be the monoadducted acetate-containing protein. The other major product at 11 292.6 Da was calculated to be a dicarboxymethylated protein. The minor peak at 11 378 Da may have corresponded to the incorporation of one acetate and one DTT molecule yielding a diadduct (expected mass is 11 384.3 Da). The other peak, at 11 173.8 Da, was due to unmodified S18C:R47C$_{red}$ protein. The spectrum of S18C:R47C exposed to iodoacetic acid in the absence of DTT (S18C:R47C$_{ox}$) is shown in Figure 4B. The major species produced from the reaction was the unmodified S18C:R47C$_{ox}$ at 11 173.8 Da. Two minor products at 11 205.5 and 11 307.8 Da may have corresponded to the addition of a potassium ion, and an acetate/β-ME diadduct (expected masses are 11 212.8 and 11 309.8 Da, respectively). The mass spectra indicated that in the absence of DTT, very little carboxymethylation occurred, as expected for an intramolecular disulfide bond predominantly in the oxidized state.

In addition to the mass spectrometry data, SDS−PAGE analysis was performed on the purified protein products from the above reactions (data not shown). Under nonreducing conditions, the oxidized disulfide-bonded protein (S18C:R47C$_{ox}$) migrated distinctly faster than both reduced (S18C:

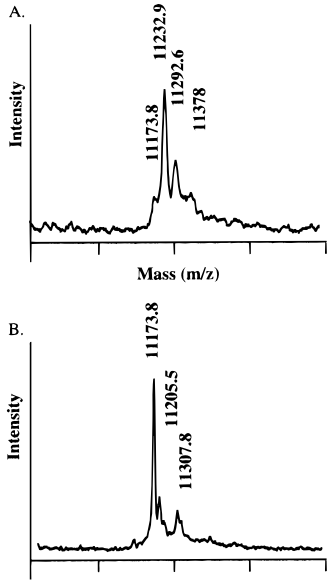

FIGURE 4: Positive-ion MALDI-TOF mass spectra of S18C:R47C cyt b_5. Matrix, 95% dihydroxybenzoic acid/5% methoxysalicylic acid; wavelength, 337 nm. S18C:R47C with iodoacetic acid and DTT (A). S18C:R47C with iodoacetic acid only (B).

$R47C_{red}$) and wild-type proteins. When β-ME was added, the S18C:$R47C_{ox}$ protein migration was similar to that of S18C:$R47C_{red}$ and wild type. These results are consistent with the expected effects of disulfide bond formation on electrophoretic mobility; that is, the oxidized disulfide-bonded protein has a smaller radius of gyration relative to its reduced counterpart and hence faster migration through the gel matrix. The oxidized disulfide bond was formed quantitatively without experimental manipulations.

Urea and Thermal Denaturation Detected by Heme Absorbance. Stability, as determined by heme dissociation, was measured by absorbance spectroscopy. Typical urea and thermal denaturation profiles are shown in Figure 5. In all cases, denaturation was followed by measuring the optical absorbance of the heme at the Soret maximum of 412 nm. Increasing the temperature or urea concentration led to a denaturant-dependent decrease in intensity and a blue-shift in the absorbance maximum. The native spectra of the wild-type and mutant proteins were indistinguishable, while the spectra for the denatured states of the proteins at 92.5 °C or 8 M urea were slightly different (data not shown).

Each urea denaturation profile of wild type or mutant cyt b_5 followed cooperative sigmoidal behavior. The urea-induced denaturation was characterized by an isosbestic point at 400 nm. The results from the thermodynamic analysis of the denaturation curves are given in Table 1. The midpoints of urea denaturation for the wild-type, S18D, and S18C:R47C proteins varied over a 0.5 M urea range, and $\Delta G_{app}(H_2O)$ values varied by 3.5 kcal/mol. Wild type exhibited the greatest stability, and S18C:$R47C_{ox}$ the lowest. Similarly, the reported m values were highest for wild type and lowest for S18C:$R47C_{ox}$.

The thermal denaturation profiles of cyt b_5 approximated a two-state transition, as previously reported for tryptic fragments of cyt b_5 (*40*−*42*). Here, thermal unfolding was partially reversible, being dependent on the exposure time at temperatures up to T_m. Isosbestic points for wild type, S18D, and S18C:$R47C_{ox}$ were observed at 395 nm, as

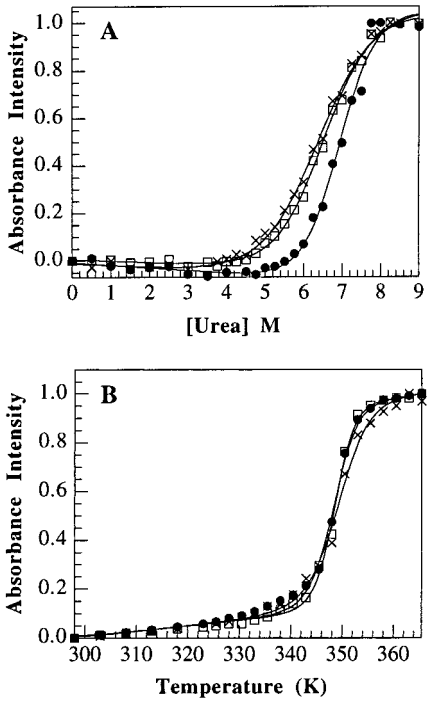

FIGURE 5: Changes in absorbance of wild-type (●), S18D (□), and S18C:$R47C_{ox}$ (×) cyt b_5 with (A) increasing urea and (B) increasing temperature. The data sets were analyzed assuming a two-state denaturation process and fit to the equations given under Materials and Methods.

Table 1: Thermodynamic Parameters for Urea and Thermal Denaturation Determined by Absorbance Spectroscopy

	Urea Denaturation[a]				
protein	$U_{1/2}$ (M)	$\Delta G_{app}(H_2O)$ (kcal/mol)	m (kcal mol^{-1} M^{-1})	χ^2	R^2
wild type	6.9	8.7	1.26	0.03	0.99
S18D	6.5	6.9	0.97	0.01	0.99
S18C/$R47C_{ox}$	6.4	5.2	0.81	0.02	0.99

	Thermal Denaturation[b]			
protein	T_m (°C)	ΔT_m (K)	χ^2	R^2
wild type	75.2	−	0.01	0.99
S18D	75.5	0.3	0.01	0.99
S18C/$R47C_{ox}$	76.0	0.8	0.01	0.99

[a] The parameters are derived from the data in Figure 5A as described in the text. The protein concentration was 10 μM for each experiment in 5 mM K_2HPO_4 at pH 7 and 25 °C. [b] The parameters are derived from the data in Figure 5B as described in the text. The protein concentration was 10 μM for each experiment in 5 mM K_2HPO_4 at pH 7. The ΔT_m values are algebraic differences in T_m for wild type and mutant.

reported previously for the wild-type protein (*40*, *41*), which further supports a two-state denaturation reaction. The thermally induced transitions were similar for the wild type and mutants, and only subtle differences in the thermodynamic parameters were observed (Table 1). The T_m values were similar for the wild type and mutants at ∼75 °C. This was close to the previously reported T_m of ∼73 °C for a similar bovine tryptic cyt b_5 fragment (residues 1−90).

Urea and Thermal Denaturation Detected by Tryptophan Fluorescence. Equilibrium stability was also determined by fluorescence spectroscopy, wherein environmental changes of Trp 22 were measured. The steady-state fluorescence spectra of wild-type and S18C:$R47C_{ox}$ forms of cyt b_5 are given in Figure 6. Denaturation was followed by measuring

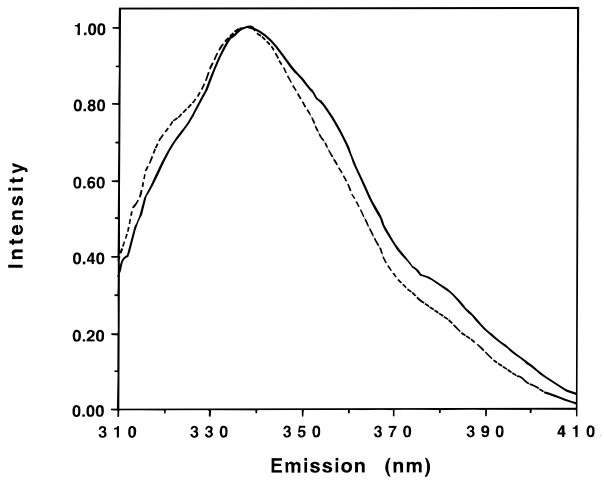

FIGURE 6: Technical steady-state fluorescence emission spectra of wild-type (solid) and S18C:R47C$_{ox}$ (dashed) cyt b_5 (excitation wavelength 295 nm). The spectra were recorded at 25 °C and normalized. The disulfide-containing mutant is blue-shifted relative to wild type.

the intrinsic fluorescence of Trp 22 at the spectral center of mass (λ_{mass}) between 310 and 370 nm and by monitoring the maximum fluorescence intensity. Under native conditions (25 °C and 0 M urea), the spectra showed subtle, reproducible differences. Notably, the wild-type emission center of mass was always red-shifted (λ_{mass} ~340 nm) relative to the mutants (λ_{mass} ~338−339 nm). Although this difference is small, it is real, and it is consistent with a more polar environment of Trp 22 in the wild type compared to the cleft-closed mutants.

The urea denaturation curves for wild-type and mutant forms of cyt b_5 determined by the emission center of mass are shown in Figure 7A. The thermodynamic parameters are shown in Table 2. Unlike the urea denaturation followed by absorbance spectroscopy, a large difference between the wild-type and mutant proteins was observed. It should be noted that while the native structures yielded fluorescence spectra different from the spectra of the denatured states, the spectra of denatured states under these conditions were essentially identical (data not presented). The native and denatured S18C:R47C$_{ox}$ fluorescence spectra were slightly blue-shifted relative to the corresponding spectra of the other proteins (Figure 6; denatured spectra not shown). The S18C:R47C$_{ox}$ protein was ~1.7 kcal/mol more stable to urea denaturing conditions than wild type. For each of the proteins, the midpoint of denaturation, based on fluorescence, occurred at much lower urea concentrations than for heme dissociation. The fluorescence intensity versus urea concentration is shown in Figure 7B. As expected, a rise in intensity was observed as the protein denatured, Trp 22 became more solvent accessible, and energy transfer from the Trp to heme became less effective. All of the proteins showed similar behavior. Initially, very little rise in intensity occurred upon addition of urea. Once the heme was no longer hexa-coordinated to the protein (*40*), a dramatic rise in intensity was observed. This rise occurred at ~5 M urea, which correlated with heme release as observed by absorbance (Figure 5A). The wild-type and S18D proteins showed slight plateaus at low urea concentrations. Unlike the aforementioned case using absorbance spectroscopy, the *m* values for the disulfide mutant were larger than wild type and S18D.

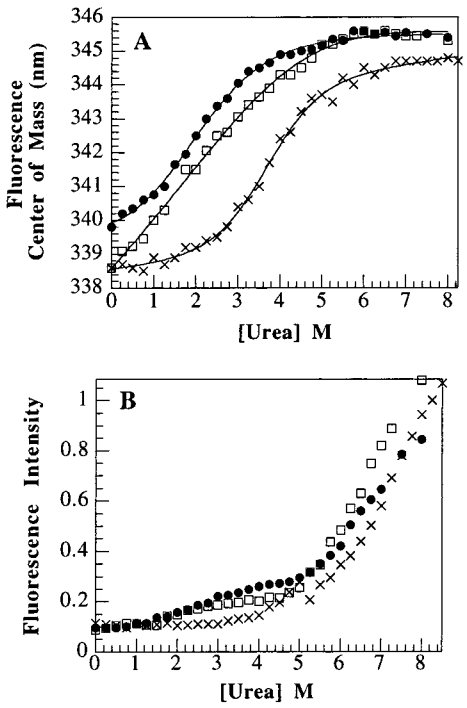

FIGURE 7: Changes in fluorescence of wild-type (●), S18D (□), and S18C:R47C$_{ox}$ (×) cyt b_5 (excitation wavelength 295 nm). (A) Fluorescence emission as a function of increasing urea. (B) Fluorescence intensity as a function of increasing urea. The data sets were analyzed assuming a two-state denaturation process and fit to the equations given under Materials and Methods.

Table 2: Thermodynamic Parameters for Urea and Thermal Denaturation Determined by Fluorescence Spectroscopy

	Urea Denaturation[a]				
protein	$U_{1/2}$ (M)	$\Delta G_{app}(H_2O)$ (kcal/mol)	*m* (kcal mol^{-1}M^{-1})	χ^2	R^2
wild type	2.3	1.7	0.73	0.52	0.99
S18D	2.5	1.4	0.56	0.61	0.99
S18C/R47C$_{ox}$	3.7	3.4	0.93	0.62	0.99

	Thermal Denaturation[b]			
protein	T_m (°C)	ΔT_m (K)	χ^2	R^2
wild type	50.1	−	0.19	0.99
S18D	52.7	2.6	0.35	0.99
S18C/R47C$_{red}$	44.8	−5.3	0.13	0.99
S18C/R47C$_{ox}$	60.8	10.7	0.24	0.99

[a] The parameters are derived from the data in Figure 7A as described in the text. The protein concentration was 10 μM for each experiment in 5 mM K_2HPO_4 at pH 7 and 25 °C. [b] The parameters are derived from the data in Figure 8A as described in the text. The protein concentration was 10 μM for each experiment in 5 mM K_2HPO_4 at pH 7.

Thermal denaturation was also monitored by fluorescence, and the data are shown in Figure 8A. As seen for the concentration dependence of urea on denaturation in fluorescence vs absorbance experiments, the T_m values determined by fluorescence occurred at much lower temperatures than observed by absorbance. Additionally, the transition region of each protein as observed by fluorescence varied. The differences are reflected in the thermodynamic analyses derived from theoretical fits to a two-state process (Table 2). T_m values were similar only for the wild-type and S18D proteins (~51 °C). The double cysteine mutant showed the greatest disparity with a T_m of ~61 °C when oxidized and ~45 °C when reduced. At extreme temperatures, a long-

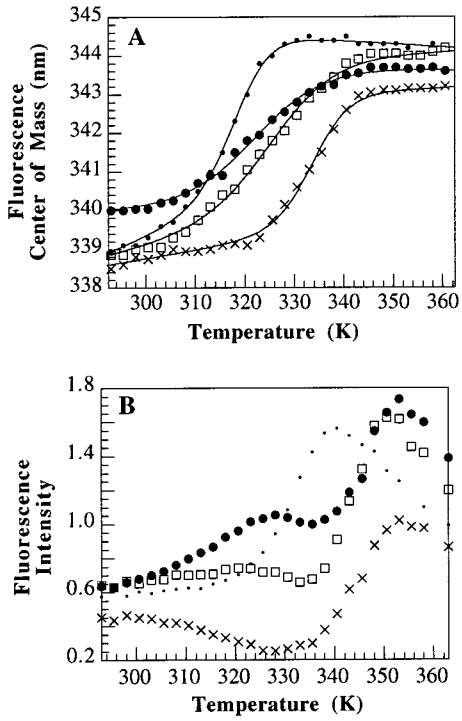

FIGURE 8: Changes in fluorescence of wild-type (●), S18D (□), S18C:R47C$_{ox}$ (×), and S18C:R47C$_{red}$ (•) cyt b_5 (excitation wavelength 295 nm). (A) Fluorescence emission center of mass as a function of increasing temperature. The data sets were analyzed assuming a two-state denaturation process and fit to the equations given under Materials and Methods. (B) Fluorescence intensity as a function of increasing temperature.

wavelength shoulder became more prominent relative to native spectra (data not shown).

In addition to the spectral center of mass, peak fluorescence intensities were followed as a function of temperature (Figure 8B). In all cases, the intensity values ultimately rose with an increase in temperature. All proteins exhibited a decrease in intensity with increasing temperature after a maximum was reached. Interestingly, the wild-type protein experienced first a slight rise, a plateau between 55 and 65 °C, and then a sharp increase. The S18D intensity paralleled this trend. Conversely, S18C:R47C$_{ox}$ showed a steady decline in intensity, before rising sharply at ~65 °C. The intensity of S18C:R47C$_{red}$ increased at ~50 °C. There was a direct correlation between the sharp rise in fluorescence intensity and the loss of heme, which occurred at similar temperatures (compare Figures 8B and 5B). Therefore, it is likely that other local fluctuations contributed to the changes in intensity and emission λ_{mass} at temperatures prior to heme release.

DISCUSSION

The goal of the studies presented here was to investigate the stability and localized dynamics of cyt b_5 through MD simulations, mutagenesis, denaturation, and fluorescence studies. These studies were motivated by the predictions from a previous MD simulation in which native ferric cyt b_5 was studied (*6*). The protein is comprised of two cores: core 1 contains the heme group and is thereby a critical functional domain, whereas core 2 is considered to be the structural scaffold and it is retained even when the heme is removed (*8*). In the simulations, large-scale fluctuations on the surface of the protein resulted in the formation of a cleft that transiently exposed the heme group and the hydrophobic interior (Figure 2) (*6*). The cleft region lies between the two cores and may be structurally important, play a role along the folding pathway, or be involved in protein recognition and electron transfer. Cyt b_5 contains spectroscopic probes in each of its cores: a heme (core 1) and Trp 22 (core 2) (Figure 1). As a result, we have used absorbance and fluorescence spectroscopies to monitor the effects in the different cores and used modeling and mutagenesis to construct two mutants designed to impair cleft dynamics. One mutant was designed to introduce a salt bridge across the cleft, and the other a covalent disulfide bond spanning the cleft. The introduction of non-native disulfide bonds can both stabilize (*43*−*48*) and destabilize proteins (*49*−*53*). In many cases, introduction of disulfide bonds leads to unexpected or uninterpretable changes in protein stability. The introduction of a de novo disulfide bond in cyt b_5 revealed interesting results regarding its equilibrium stability. First, we discuss the MD simulations and the structural information they provide relating to conformational stability. Then, we present the characterization of the mutants through denaturation studies. Finally, we discuss the effects of mutations on the equilibrium of what appears to be two essentially native conformational substates (*N* to *N*′) prior to heme loss.

MD Simulations. We performed MD simulations at 25 and 50 °C in order to compare protein structure and dynamics in the native state and at a point along the thermal denaturation pathway before loss of heme. Specifically, we were interested in the structural implications of the mutations on the putative cleft region and other areas of the protein. There was an area of localized motion in the wild-type simulation that encompassed the cleft region. This motion became even more dramatic as the temperature was increased to 50 °C and the open form became more populated. This ensemble of structures was more representative of a 'cleft-opened' conformer. The flexibility in the region between α-helices 2 and 3 was important for progression to the more dynamic structures seen at 50 °C. At 25 °C, the S18D structure fluctuated very little except at the termini, due to the constraint imposed by the S18D−R47 salt bridge. At 50 °C, the S18D−R47 salt bridge was broken, and the dynamic behavior was similar to that of wild type. In the S18C:R47C$_{ox}$ simulation, the fluctuations in the cleft region were damped relative to the wild type and remained so even at 50 °C. The resulting ensemble resembled the wild-type 'cleft-closed' conformation. The S18C:R47C$_{red}$ simulation, however, revealed the most unexpected results. In this simulation, the introduction of the R47C mutation introduced a 'kink' in the segment between α-helices 2 and 3, preventing fluctuations in the cleft region as observed in the wild-type protein. Even at 50 °C, the 'kink' inhibited motion in this area, resulting in a more nativelike conformation. However, increased dynamics in α-helix 1 and the adjacent loop were observed, as in the wild-type simulation. The experimental results showed that the thermal transition occurred earlier for S18C:R47C$_{red}$ and appeared to be more cooperative than for the other proteins, based on the qualitative steepness of the transition. Due to difficulty in preparing S18C:R47C$_{red}$ without heterogeneity at the level of carboxymethylation, not all denaturation experiments were performed with this variant.

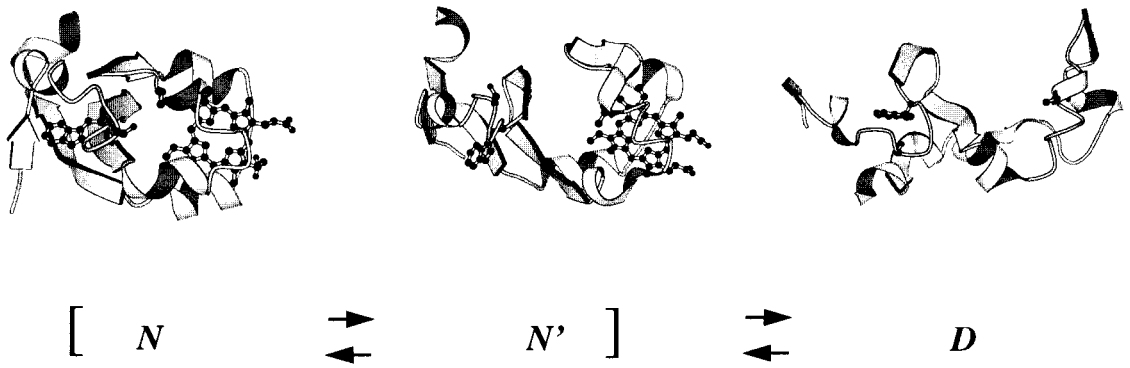

FIGURE 9: Main-chain C_α traces of wild-type cyt b_5 at different points along the denaturation pathway as described by the model presented in the text. Orientations are the same as in Figure 1. The native structure (*N*) was obtained from the holocyt b_5 simulation (*6*). The native substate (*N*′) was generated from the 50 °C simulation presented in this paper and reflects an exaggerated 'cleft-opened' conformation. The denatured state (*D*) was obtained from a 225 °C MD simulation performed without the heme present (unpublished data).

Effects of Mutation on Heme Binding. Mutational effects on protein stability, specifically between the native and denatured states, *N* to *D*, were monitored through changes in heme absorbance. In all cases, the results showed a single cooperative transition between the compact folded state and the more disordered, denatured state. The thermal denaturation results showed very little variation upon introduction of the mutations. However, the effects of urea on heme dissociation were more pronounced. Wild-type cyt b_5 was the most stable species under these conditions. On the basis of heme dissociation, the wild-type protein was 1.8−3.5 kcal/mol more stable than the variants. In addition, based on *m* values, transition midpoints were differentially sensitive to urea. The *m* values usually decrease as a protein is constrained by covalent cross-links due to a decreased solvent-accessible surface area of the denatured state (*54*). Both mutants showed smaller *m* values relative to the wild-type protein. Although these results were interesting, absorbance spectroscopy did not reveal structural changes around the heme at low denaturant concentrations.

Although the data were analyzed considering a two-state model for unfolding, as others have done in the past, we noticed that they were poorly fit by the theoretical curves, particularly at low denaturant concentrations (Figure 5). The denaturation results obtained by fluorescence, however, shed light on structural events that may contribute to these poor fits.

Mutant Effects at the Interface of Cores 1 and 2. Fluorescence spectroscopy is very sensitive to changes in environment and solvent accessibility and, therefore, is a good probe of structural dynamics and changes in tertiary structure. The side chain of Trp 22 is contained within core 2, while the main chain is also in direct contact with core 1. Any solvent accessibility of the Trp 22 side chain through core 2 fluctuations was expected to remain similar in the wild type and mutants because of the structural rigidity of this domain. Even in the absence of heme, core 2 remains very structured, maintaining all of the native Trp 22 NOE contacts of the holoprotein (*8, 11, 13*). Differences in solvent penetration through the core 1/core 2 cleft region, however, should be affected by the mutations and could be monitored by fluorescence. As observed in the wild-type cyt b_5 MD simulation, the cyclical formation and closure of the cleft allows solvent accessibility of the Trp 22 main chain through this route (*6*), not accessible to the S18D and S18C:R47C_{ox} mutants designed to prevent 'cleft opening'. In our steady-state fluorescence results of wild-type cyt b_5 and mutants, we observed subtle but reproducible differences in the intrinsic fluorescence (Figure 6). The λ_{mass} of the wild-type protein was red-shifted relative to the mutants. S18C:R47C_{ox} was the most blue-shifted. These differences reflect the environment of Trp 22 and are attributed to decreased solvent accessibility through the cleft region due to mutations designed to form the 'cleft-closed' conformation (Figure 2).

Unlike the results obtained from absorbance spectroscopy, fluorescence revealed large alterations in conformational equilibria in the wild-type and mutant proteins prior to heme release (summarized in Table 2). By the time heme release occurred, all denaturant-related events monitored by fluorescence were complete. The thermodynamic parameters in Table 2, which differ significantly from those in Table 1, appear to reflect the equilibrium between two native state conformers: *N* and *N*′ (Figure 9). The introduction of the disulfide cross-link across the protein cleft affected the *N* to *N*′ equilibrium by preventing the formation of *N*′ and increasing the transition temperature by ∼11 °C, as measured by fluorescence. Conversely, when the disulfide bond was broken, the protein was destabilized relative to wild type by ∼5 °C, giving a 16 °C difference in T_m between the oxidized and reduced disulfide mutants. The introduction of the free carboxymethylated sulfhydryls offers little stabilization of the 'cleft-closed' conformation. In the wild-type protein, Arg 47 transiently hydrogen bonds to the δ-oxygen of Ser 18. The lack of this interaction in S18C:R47C_{red} leads to destabilization of the *N* state. The R47C mutation also affected conformational flexibility between α2 and α3. Hence, in S18C:R47C_{red}, progression to *N*′ was affected and the preferred equilibrium conformer was *N, a conformation*. Introduction of the salt bridge in the S18D mutant had modest effects on conformational equilibria, but the observed differences were consistent with an engineered salt bridge leading to decreased preference for the 'cleft-open' or *N*′ conformation.

Differences between Absorbance and Fluorescence Results Prior to Heme Release. Interestingly, for each protein, absorbance and fluorescence revealed different transition points. More denaturant was required to reach the T_m when heme absorbance was monitored than when the tryptophan environment was monitored. This indicated that the most dramatic differences in fluorescence occurred and were

complete prior to heme dissociation (Figures 7B and 8B). Presumably, several factors contributed to the fluorescence changes, such as quenching due to energy transfer to the heme, changes in solvent accessibility, and differences in the interactions between the excited-state dipole of the fluorophore and nearby polar residues.

The fluorescence intensity profiles prior to heme release were complex. Our structural interpretations based on these results were aided by the MD simulations at 25 and 50 °C. Urea had modest effects on fluorescence intensity prior to heme release. Both wild type and S18D, however, showed slight plateaus at low urea concentrations. At temperatures prior to heme dissociation, the intensity profile of each protein was quite different. For the wild-type and S18D proteins, a pronounced plateau was reached. We interpret this as the favored formation of a native substate (N') corresponding to an increased population of the 'cleft-open' conformation (Figure 2). The plateau was completely absent in the S18C:R47C_{ox} protein. It is proposed that the covalent 'tether' in the disulfide-bonded protein prevented formation of N', and the protein remained in a 'cleft-closed' conformation until heme release occurred.

Taken together, the temperature and urea dependence of fluorescence emission wavelength and intensity depicts a more complex denaturation scheme than just a simple release of heme concomitant with loss of structure. The differences in transition regions between the absorbance and fluorescence denaturation curves reflected structural changes that occurred at two different points along the denaturation pathway. The absorbance data showed the effects of denaturant on heme release occurring at large concentrations of urea or high temperatures; the transition region of heme release began at 65 °C or 5 M urea. However, the fluorescence data suggest that significant structural perturbations occurred at temperatures or urea concentrations lower than those required to cause heme release. At 65 °C, nearly all of the spectral perturbations of fluorescence intensity or emission wavelength were complete. In contrast, formation of this conformational ensemble present at low temperature or urea concentration was insignificant in the S18C:R47C_{ox} mutant.

The results from the thermal and urea denaturation of wild-type and mutant forms of cyt b_5 can be described by a modified two-state model involving native holoprotein (N), an alternate nativelike conformational substate favoring the 'cleft-opened' conformer (N'), and denatured apoprotein (D) shown in Figure 9. The denaturation results of this study suggest that some structural rearrangement occurs during the early stages of the denaturation process before heme is released and that a simple two-state model cannot fully describe cyt b_5 denaturation. The fluorescence intensity results suggest that N' is structurally more similar to the native state N than the denatured state D. The equilibrium between N and N' is affected by a strategically placed de novo salt bridge or disulfide bond. Although our denaturation results do not allow the different conformational states to be characterized directly, they are consistent with our MD-generated data, which show limited structural differences between the N and N' states that are concentrated in one region—the cleft. Thus, moderate perturbants appear to increase the population of the conformer with the cleft opened. In the accompanying manuscript (*58*), we further characterize the mutational effects on local structure near the cleft.

ACKNOWLEDGMENT

We gratefully acknowledge Drs. Kheng Lim and Murray Hackett for performing the MALDI-TOF MS experiments. We thank Michael J. Dabrowski and Dr. Raimund M. Peter for providing helpful comments on the mutagenesis procedures and Dr. Darwin O.V. Alonso for suggestions regarding the stability studies. We also thank Dr. Juliette T. J. Lecomte for many helpful discussions and critical comments on the manuscript. The molecular graphics images in Figures 2 and 3 were produced using the UCSF MidasPlus program from the Computer Graphics Laboratory, University of California, San Francisco (supported by National Institutes of Health Grant RR-01081) (*55*, *56*). Figures 1 and 9 were constructed using the Molscript program (*57*).

REFERENCES

1. Hultquist, D. E., and Passon, P. G. (1971) *Nature (London), New Biol. 229*, 252−254.
2. Hultquist, D. E., Dean, R. T., and Douglas, R. H. (1974) *Biochem. Biophys. Res. Commun. 60*, 28−34.
3. Okayasu, T., Ono, T., and Shinogima, K. (1977) *Lipids 12*, 267−271.
4. Strittmatter, P., Spatz, L., Corcoran, D., Rogers, M. J., Setlow, B., and Redline, R. (1974) *Proc. Natl. Acad. Sci. U.S.A. 71*, 4565−4569.
5. Bernardi, P., and Azzone, G. F. (1981) *J. Biol. Chem. 256*, 7187−7192.
6. Storch, E. M., and Daggett, V. (1995) *Biochemistry 34*, 9682−9693.
7. Arnesano, F., Banci, L., Bertini, I., and Felli, I. C. (1998) *Biochemistry 37*, 173−184.
8. Moore, C. D., and Lecomte, J. T. J. (1990) *Biochemistry 29*, 1984−1989.
9. Lecomte, J. T. J., and Moore, C. D. (1991) *J. Am. Chem. Soc. 113*, 9663−9665.
10. Moore, C. D., Al-Misky, O. N., and Lecomte, J. T. J. (1991) *Biochemistry 30*, 8357−8365.
11. Moore, C. D., and Lecomte, J. T. J. (1993) *Biochemistry 32*, 199−207.
12. Falzone, C. J., Mayer, M. R., Whiteman, E. L., Moore, C. D., and Lecomte, J. T. J. (1996) *Biochemistry 35*, 6519−6526.
13. Storch, E. M., and Daggett, V. (1996) *Biochemistry 35*, 11596−11604.
14. Salemme, F. R. (1976) *J. Mol. Biol. 102*, 563−568.
15. Poulos, T. L., and Mauk, A. G. (1983) *J. Biol. Chem. 258*, 7369−7373.
16. Livingston, D. J., McLachlan, S. J., Mar, G. N. L., and Brown, W. (1985) *J. Biol. Chem. 260*, 15699−15707.
17. Mauk, M. R., Mauk, A. G., Weber, P. C., and Matthew, J. B. (1986) *Biochemistry 25*, 7085−7091.
18. Wendoloski, J. J., Matthew, J. B., Weber, P. C., and Salemme, F. R. (1987) *Science 238*, 794−797.
19. Stayton, P. S., Poulos, T. L., and Sligar, S. G. (1989) *Biochemistry 28*, 8201−8205.
20. Ng, S., Smith, M. B., Smith, H. T., and Millet, F. (1977) *Biochemistry 16*, 4975−4978.
21. Tamburini, P. P., White, R. E., and Schenkman, J. B. (1985) *J. Biol. Chem. 260*, 4007−4015.
22. Rodgers, K. K., Pochapsky, T. C., and Sligar, S. G. (1988) *Science 240*, 1657−1659.
23. Mauk, M. R., and Mauk, A. G. (1989) *Eur. J. Biochem. 186*, 473−486.
24. Rodgers, K. K., and Sligar, S. G. (1991) *J. Mol. Biol. 221*, 1453−1460.
25. Mathews, F. S., Argos, P., and Levine, M. (1972) *Cold Spring Harbor Symp. Quant. Biol. 36*, 387−395.

26. Levitt, M. (1990) *ENCAD−Energy Calculation and Dynamics*, Molecular Applications Group, Palo Alto, CA.
27. Levitt, M., Hirshberg, M., Sharon, R., and Daggett, V. (1995) *Comput. Phys. Commun. 91*, 215−231.
28. Levitt, M., Hirshberg, M., Sharon, R., Laidig, K. E., and Daggett, V. (1997) *J. Phys. Chem. B 101*, 5051−5061.
29. Daggett, V., and Levitt, M. (1992) *Proc. Natl. Acad. Sci. U.S.A. 89*, 5142−5146.
30. Henry, E. R., Levitt, M., and Eaton, W. A. (1985) *Proc. Natl. Acad. Sci. U.S.A. 82*, 2034−2038.
31. Kell, G. S. (1967) *J. Chem. Eng. Data 12*, 66−69.
32. Beck von Bodman, S., Schuler, M. A., Jollie, D. R., and Sligar, S. G. (1986) *Proc. Natl. Acad. Sci. U.S.A. 83*, 9443−9447.
33. Stayton, P. S., Fisher, M. T., and Sligar, S. G. (1988) *J. Biol. Chem. 263*, 13544−13548.
34. Sambrook, J., Fritsch, E. F., and Maniatis, T. (1989) in *Molecular Cloning: A Laboratory Manual*, Cold Spring Harbor Laboratory Press, Cold Spring Harbor, NY.
35. Visser, L., Robinson, N. C., and Tanford, C. (1975) *Biochemistry 14*, 1194−1199.
36. Coligan, J. E., Dunn, B. M., Ploegh, H. L., Speicher, D. W., and Wingfield, P. T. (1996) in *Current Protocols in Protein Science 15.1.3*., John Wiley & Sons, Inc., New York.
37. Pace, C. N. (1986) *Methods Enzymol. 131*, 266−280.
38. Agashe, V. R., and Udgaonkar, J. B. (1995) *Biochemistry 34*, 3286−3299.
39. Wüthrich, K. (1986) in *NMR of Proteins and Nucleic Acids*, pp 111−113, John Wiley & Sons, Inc., New York.
40. Kitagawa, T., Sugiyama, T., and Yamano, T. (1982) *Biochemistry 21*, 1680−1686.
41. Newbold, R. J., Hewson, R., and Whitford, D. (1992) *FEBS Lett. 314*, 419−424.
42. Hewson, R., Newbold, R. J., and Whitford, D. (1993) *Protein Eng. 6*, 953−964.
43. Matsumura, M., Signor, G., and Matthews, B. W. (1989) *Nature 342*, 291−293.
44. Takagi, H., Takahashi, T., Momose, H., Inouye, M., Maeda, Y., Matsuzawa, H., and Ohta, T. (1990) *J. Biol. Chem. 265*, 6874−6878.
45. Kanaya, S., Katsuda, C., Kimura, S., Nakai, T., Kitakuni, E., Nakamura, K., Katayanagi, H., Morikawa, K., and Ikehara, M. (1991) *J. Biol. Chem. 266*, 6038−6044.
46. Wakarchuk, W. W., Sung, W. L., Campbell, R. L., Cunningham, A., Watson, D. C., and Yaguchi, M. (1994) *Protein Eng. 7*, 1379−1386.
47. Clarke, J., Henrick, K., and Fersht, A. R. (1995) *J. Mol. Biol. 253*, 493−504.
48. Mansfeld, J., Vriend, G., Dijkstra, B. W., Veltman, O. R., Van den Berg, B., Venema, G., Ulbrich-Hofmann, R., and Eijsink, V. G. H. (1997) *J. Biol. Chem. 272*, 11152−11156.
49. Wells, J. A., and Powers, D. B. (1986) *J. Biol. Chem. 261*, 6564−6570.
50. Villafranca, J. E., Howell, E. E., Oatley, S. J., Xuong, N. H., and Kraut, J. (1987) *Biochemistry 26*, 2182−2189.
51. Mitchinson, C., and Wells, J. A. (1989) *Biochemistry 28*, 4807−4815.
52. Van den Burg, B., Dijkstra, B. W., Van der Vinne, B., Stulp, B. K., Eijsink, V. G. H., and Venema, G. (1993) *Protein Eng. 6*, 521−527.
53. Betz, S. F., Marmorino, J. L., Saunders, A. J., Doyle, D. F., Young, G. B., and Pielak, G. J. (1996) *Biochemistry 35*, 7422−7428.
54. Shortle, D. (1995) *Adv. Protein Chem. 46*, 217−247.
55. Ferrin, T. E., Huang, C. C., Jarvis, L. E., and Langridge, R. (1988) *J. Mol. Graphics 6*, 13−27.
56. Huang, C. C., Pettersen, E. F., Klein, T. E., Ferrin, T. E., and Langridge, R. (1991) *J. Mol. Graphics 9*, 230−236.
57. Kraulis, P. (1991) *J. Appl. Crystallogr. 24*, 946−950.
58. Storch, E. M., Grinstead, J. S., Campbell, A. P., Daggett, V., and Atkins, W. M. (1999) *Biochemistry 38*, 5065−5075.

BI982158Q